OPEN ACCESS

ARTICLE

A preliminary study on graphical method of thermodynamic process parameters under dynamic boundary conditions

Kunteng Huang,[1] Zhixin Huang,[1] Ruihua Chen,[1] Ruizhao Gao,[1] Hao Wang,[1] Weicong Xu,[1] Shuai Deng,[1] and Li Zhao[1,*]

*Correspondence: jons@tju.edu.cn (L. Z.)

Received: October 4, 2024; Accepted: December 2, 2024; Published Online: April 4, 2025; https://doi.org/10.59717/j.xinn-energy.2025.100084

GRAPHICAL ABSTRACT

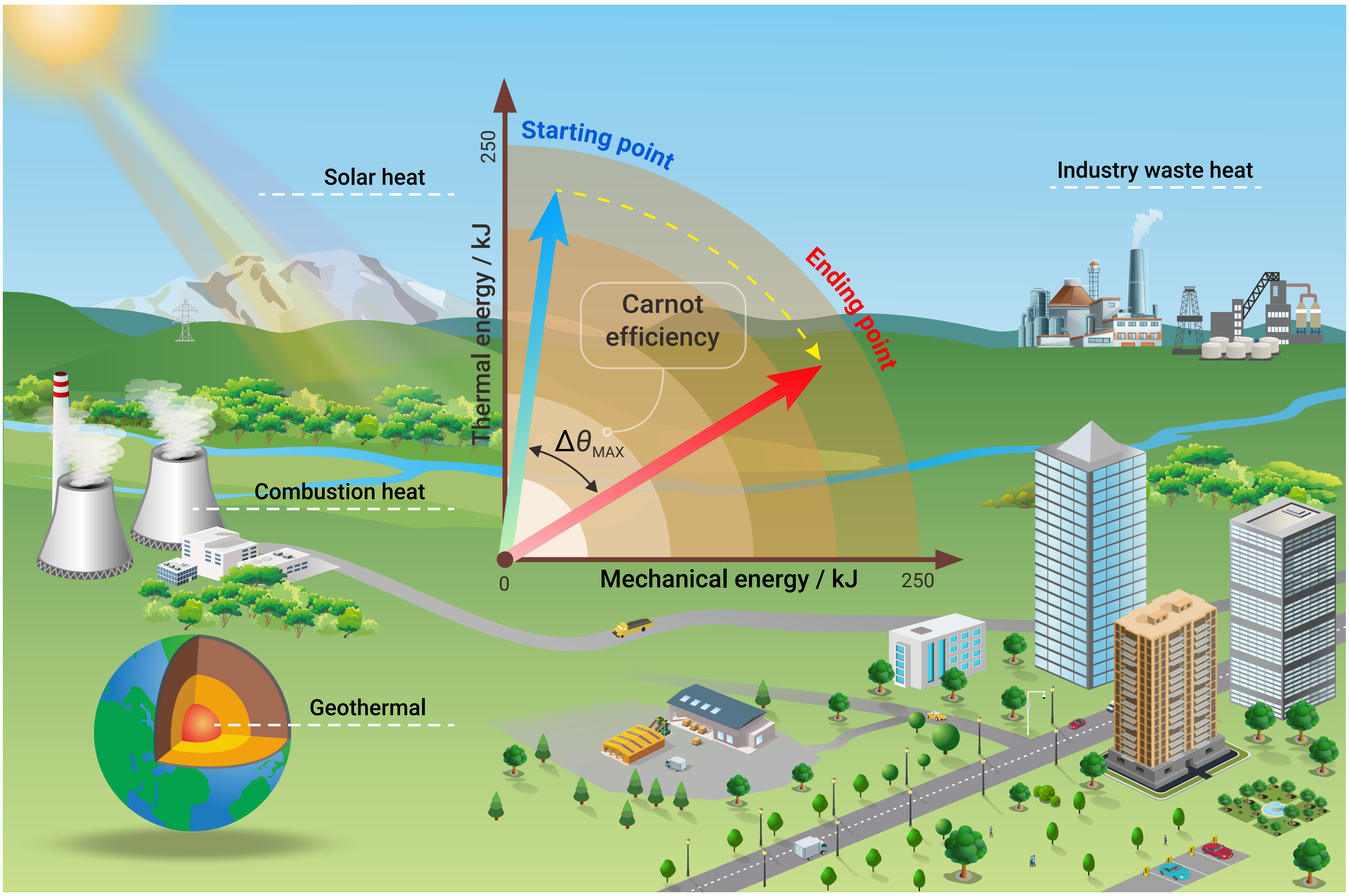

PUBLIC SUMMARY

- Novel representation of thermodynamic laws through radius rotation in a circle.
- Geometric parameters effectively describe system performance at all scales.
- Coupled analysis method applicable across various energy conversion devices.
- New dimension enables insights into multi-energy conversion processes.

A preliminary study on graphical method of thermodynamic process parameters under dynamic boundary conditions

Kunteng Huang,[1] Zhixin Huang,[1] Ruihua Chen,[1] Ruizhao Gao,[1] Hao Wang,[1] Weicong Xu,[1] Shuai Deng,[1] and Li Zhao[1,*]
[1]State Key Laboratory of Engines, Tianjin University, Tianjin, China
*Correspondence: jons@tju.edu.cn (L. Z.)

Received: October 4, 2024; Accepted: December 2, 2024; Published Online: April 4, 2025; https://doi.org/10.59717/j.xinn-energy.2025.100084

Citation: Huang K., Huang Z., Chen R., et al. (2025). A preliminary study on graphical method of thermodynamic process parameters under dynamic boundary conditions. *The Innovation Energy* **2**:100084.

Thermodynamic graphical methods are useful tools for visualizing thermodynamic state equations and are widely applied in the design and optimization of thermodynamic systems. However, the integration of renewable energy and thermal storage systems introduces finite heat capacity characteristics, resulting in continuous dynamic variations in system performance, which poses challenges to existing graphical methods. To accurately describe system performance under dynamic boundary conditions, this study investigates the continuous analysis characteristics of the Energy-Energy (*E-E*) diagram. Based on the ideal gas model, mathematical expressions for thermal and mechanical energy are derived, and systematic comparisons between *E-E* and Temperature (*T*)-Entropy (*s*) diagrams under finite heat capacity conditions are conducted, elucidating the intrinsic relationships among geometric parameters, initial boundary conditions, and system performance. Through parametric analysis, we reveal that increasing the initial heat reservoir temperature from 500 K to 1500 K enhances the energy conversion potential, with the rotation angle increasing from 20.77° to 37.15°. Additionally, increasing the heat reservoir to cold reservoir capacity ratio results in a decreased rotation angle, indicating lower efficiency. The *E-E* diagram achieves visualization by analogizing energy conversion processes to the rotational motion of a radius in a circle. Compared to the *T-s* diagram, it employs lines and slopes instead of areas and area ratios, exhibiting advantages in analyzing varying boundary conditions. This complementary coupling provides a new perspective for describing dynamic energy conversion processes in thermodynamic systems.

INTRODUCTION

Energy conversion is an inevitable process of power generation and energy storage.[1-3] With the rapidly increasing demand for environmental sustainability, there is a need of transition from a high-carbon era to a low-carbon or even zero-carbon era.[4,5] Utilizing renewable energy is an effective way to achieve energy savings and carbon reduction, and the energy conversion pathway is one of the critical factors for the efficient utilization of renewable energy.[6] Taking the solar-powered hydrogen production process via hydrolysis as an example, solar energy can be used directly for photocatalytic water splitting, converted into electrical energy for electrolysis, or transformed into thermal energy for high-temperature thermolysis to produce hydrogen.[7-9] In different energy conversion pathways, the evolution of system irreversibility varies, which has a significant impact on the operational efficiency of the components.[10,11] The key to high efficiency utilization of renewable energy lies in achieving cascaded energy utilization during the energy conversion process.[12,13]

To explore the intrinsic relationships between operating parameters and the performance of energy conversion devices, graphical methods offer an effective approach and have been widely applied in fields such as thermal power generation,[14,15] refrigeration and heat pump systems,[16,17] fluid heat transfer processes[18-21] and energy storage technologies.[22-25] These graphical methods serve two main categories: First, diagrams representing characteristic parameters and dimensionless parameters,[26-29] where changes in geometric features like angles and slopes help assess the fluid physical and flow characteristics. Second, thermodynamic state parameters (e.g. temperature-entropy, pressure-volume, and pressure-enthalpy diagrams), which effectively visualize fundamental thermodynamic state equations, enable comparison between ideal and actual heat-work conversion devices, and facilitating the analysis of energy conversion irreversibility. Such methods form the basis for guiding the structural design.[30-32] Moreover, a defining feature of thermodynamic graphical methods is that the two coordinates are the decomposing parameters from the thermodynamic process parameters, that is, an intensive parameter and an extensive parameter respectively.[33-35] By integrating the changes between these parameters (area), expressions for heat and work quantities are derived, after which system performance can be evaluated by comparing the areas. Similarly, for other forms of energy conversion, such as chemical-to-electrical energy or thermal-to-chemical energy, the thermodynamic process parameters can also be decomposed and used as coordinates in graphical analysis.[36,37] However, these graphical methods are primarily used for analyzing steady-state processes.

For a dynamic boundary, such as the sensible heat storage or release process in a Carnot battery's thermal storage tank,[38,39] the temperature of the storage medium continuously changes during operation lead to the change in the working fluid's state within the thermodynamic cycle. Using thermodynamic state parameter graphical methods to illustrate system performance variations will result in discontinuities in the area, making it difficult to intuitively represent the performance variations of the heat-work conversion process. Therefore, existing studies prefer to choose temperature (*T*)-entropy (*s*) diagram at specific moment for graphical. However, this method often overlooks the variations in pinch point locations during the phase change of cold/hot reservoir and fails to demonstrate the ideal performance changes throughout the entire heat power conversion process. These limitations have become increasingly significant as thermodynamic systems increasingly incorporate dynamic thermal storage processes and renewable energy integration. There is therefore an urgent need for new graphical methods capable of analyzing energy conversion processes under dynamic boundary conditions, particularly for optimizing the design and operation of advanced energy storage and conversion systems.

As previously mentioned, thermodynamic process parameters are continuous integrals of state variables. When using process parameters as the coordinates for graphical analysis, the area representing the process parameters can be reduced dimension to a line, which holds great potential for system performance characterization under dynamic boundary conditions. Based on this, in this study, we focus on the Energy-Energy (*E-E*) diagram, which visualizes the energy conversion process from a system energy perspective. By analogizing the energy conversion process to the rotation of a circle's radius, the rotational angle is correlated with energy conversion efficiency. To demonstrate the application of the *E-E* diagram, the conversion between thermal energy and mechanical energy is used as an example for analysis, with a comparison of the advantages and disadvantages of the *E-E* diagram and the *T-s* diagram. Additionally, the different of graphical geometry parameters in the *E-E* diagrams under varying initial thermal reservoir temperatures and different initial energy distributions are also investigated. The *E-E* diagram offers a novel perspective for the design and optimization of energy conversion processes.

METHODS

Principles of *E-E* diagram. To gain a deeper understanding of the characteristics of graphical methods under dynamic boundary conditions, the *E-E* diagram[40] is selected as the research object. Compared to the existing graphical method that use fundamental thermodynamic state parameters as coordinates, the *E-E* diagram is a graphical method from the perspective of energy distribution, which is taking the different forms of energy as coordinate parameters, as shown in Figure 1. According to the 1st Law of Thermodynamics, when energy is converted between any two basic energy forms (thermal energy, mechanical energy, chemical energy, and electrical energy, etc.), the total energy involved in the conversion process (E_{total}) remains constants. That is to say, energy can only transform from one form (E_1) to another form (E_2) without disappearing or appearing out of nowhere. Interestingly, a similar characteristic can be found in the geometric structure of a circle, where the radius length (r) remains constant during rotation, and the rotation degree can be represented by the rotation angle (θ) of the circle. Therefore, based on this characteristic, the energy conversion process presents in the *E-E* diagram can be viewed as the rotational process of a radius around a circle, that is, $E_{total}=r$, and the trajectory of the energy conversion process continuously changes along the red arc. For the system state of starting point (point *a*) and the ending point (point *b*) in energy conversion process, the rotation angles (θ_a and θ_b) are different, thus representing different system energy distributions. It is worth mentioning that, according to trigonometric functions, the coordinates of points *a* and *b* are ($r\sin\theta_a$, $r\cos\theta_a$) and ($r\sin\theta_b$, $r\cos\theta_b$) respectively. The sum of the horizontal and vertical coordinates of system state is not equal to r, but equal to $r(\sin\theta+\cos\theta)$, which indicates that the coordinates of system state are not equal to the system's energy distribution but are the energy distribution multiplied by a coefficient (ψ) related to θ ($\psi=\sin\theta+\cos\theta$). Hence, E_1 and E_2 can be expressed by the geometric parameters on the *E-E* diagram, as shown in Equations (1)-(2). Then the coordinates of points *a* and *b* can be rewritten as ($E_{2,a}\psi_a$, $E_{1,a}\psi_a$) and ($E_{2,b}\psi_b$, $E_{1,b}\psi_b$).

$$E_1 = \frac{r\cos\theta}{\psi} \tag{1}$$

$$E_2 = \frac{r\sin\theta}{\psi} \tag{2}$$

For energy distribution of the system, the relationship between E_1 and E_2 is satisfies Equation (3), which presents as a line with a slope (k) of -1 on the *E-E* diagram (blue dashed line). Moreover, for any system state point *a*, it lies on the same straight line as the energy distribution point *a*' and the center of a circle *O*, meaning that point *a*' is a point on the radius r_a. This is because, for a given θ, the ratio of the horizontal coordinate to the vertical coordinate for both points *a* and *a*' is equal to the tangent of θ ($\tan\theta$), indicating a geometric relationship between the blue dashed line and the red arc, as shown in Equation (4).

$$E_1 + E_2 = E_{total}\,(constant) \tag{3}$$

$$\tan\theta = \frac{E_2}{E_1} \tag{4}$$

To quantitatively evaluate the efficiency of the conversion from E_1 to E_2, the energy conversion efficiency (η_{con}) is commonly used, which is defined as the ratio of the conversion energy (ΔE_1) to the initial energy (E_1). Furthermore, according to Equations (1)-(2), η_{con} can be described using geometric parameters, as shown in Equation (5). Moreover, since the ratio of $\cos\theta_b$ to ψ_b is a monotonically decreasing function within the interval [0, 90°]. Therefore, under the same initial energy distribution, the higher the θ_b, the higher the η_{con}. For different sets of energy conversion devices, the energy conversion efficiency of the system can be intuitively comparison through the rotation angle of the *E-E* diagram.

$$\eta_{con} = 1 - \frac{1+\tan\theta_a}{1+\tan\theta_b} \tag{5}$$

Graphical representation of the energy conversion from thermal energy to mechanical energy. Among various forms of energy, the conversion between thermal energy and mechanical energy is the most commonly seen process. To gain a deeper understanding of the characteristics of the *E-E* diagram, the process of thermal energy (E_T) converted into mechanical energy (E_M) is taken as an example to explored, as shown in Figure 2A. Ideally, the heat-work conversion of an ideal gas is through the expansion of gas. The energy conversion system requires at least a heat reservoir (E_H), a cold reservoir (E_C), and a mechanical energy storage reservoir. During energy conversion, a portion of the high energy grade of thermal energy (ΔE_H) in the heat reservoir is converted into mechanical energy (ΔE_M), while the remaining unconverted thermal energy is transferred into the cold reservoir (ΔE_C). As these three reservoirs form an isolated system, the total energy within the system (E_{total}) remains constant. Moreover, due to the infinite heat capacity of the ideal gas in the heat and cold reservoirs, the temperature within the reservoirs variations as the energy conversion process progresses.

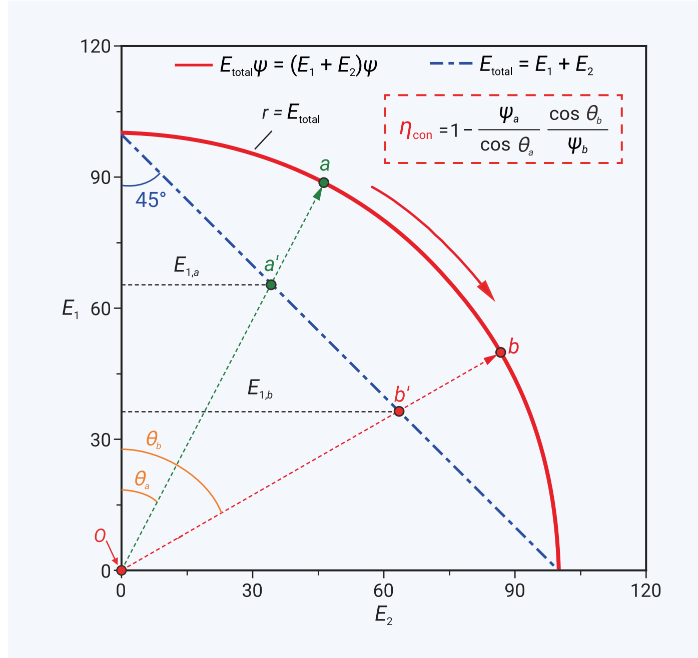

Figure 1. Principles of *E-E* diagram

In an energy conversion system, thermal energy consists of two reservoirs: a heat reservoir and a cold reservoir. Therefore, according to the energy balance equations, $E_T = E_H + E_C$ can be obtained. Moreover, the thermal energy of ideal gas is related to the mass and specific enthalpy,[35] as shown in Equations (6)-(7).

$$E_H = m_H h_H \tag{6}$$

$$E_C = m_C h_C \tag{7}$$

where m_H and m_C are the mass of ideal gas in high-temperature reservoir and low-temperature reservoir respectively; h_H and h_C are the specific enthalpy of ideal gas in high-temperature reservoir and low-temperature reservoir respectively. For an ideal gas, h is solely related to the specific heat capacity at constant pressure (c_P), the absolute temperature (T), and the reference temperature (T_0),[41] as expressed in Equation (8).

$$h = c_P (T - T_0) \tag{8}$$

The value of c_P depends on the type of ideal gas. For an ideal gas composed of monoatomic particles, each atom has three degrees of freedom. According to the equipartition theorem,[42] the kinetic energy for each degree of freedom is $\frac{1}{2}k_B T$ (where k_B is the Boltzmann constant, 1.380649×10^{-23} J/K). Moreover, according to the definition of internal energy ($u = \frac{3}{2}N_A k_B T = \frac{3}{2}RT$), the definition of specific heat capacity at constant volume ($c_v = \left(\frac{du}{dT}\right)_v$) and the Mayer's relation[43] ($c_P - c_v = R$), c_P can be derived, as shown in Equation (9).

$$c_P = \frac{5}{2}R \tag{9}$$

For mechanical energy storage reservoir, E_M is related to the pressure (P_M), specific volume (v_M), and the mass of ideal gas in storage reservoir (m_M),[44] as expressed:

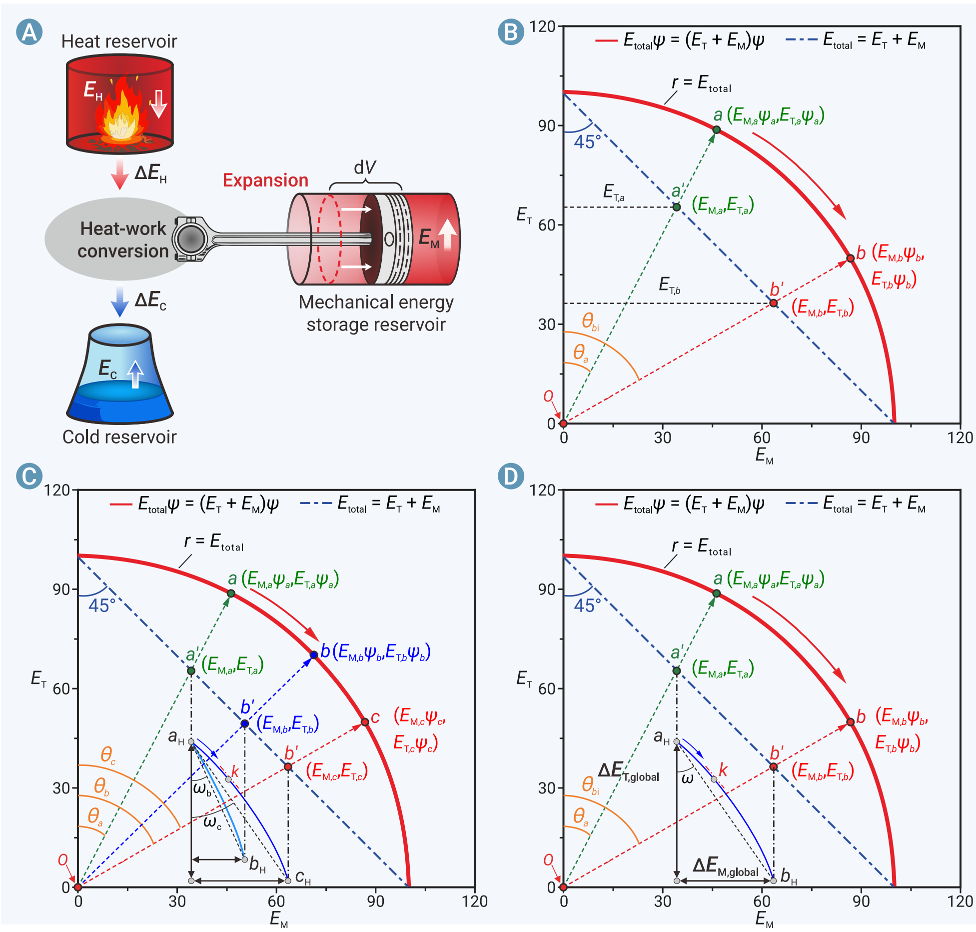

Figure 2. Schematic and graphical representation of heat-work conversion process (A) Schematic of thermal energy convert into mechanical energy; Geometry parameters of E-E diagram: (B) Global parameters, (C) Local parameters and (D) Comparison between actual working conditions and ideal working conditions.

$$E_M = m_M P_M dv_M \tag{10}$$

As the heat-work conversion progress, the energy distribution correspondingly varies. For a reversible system with finite heat capacity, the global thermal efficiency ($\eta_{\text{therm,global}}$) is related to the average temperature of the heat reservoir ($T_{\text{H,ave}}$) and cold reservoir ($T_{\text{C,ave}}$) due to the varying temperatures, as shown in Equation (11). Similarly, in any moment of energy conversion process, the local thermal efficiency ($\eta_{\text{therm,local}}$) is related to the local heat reservoir temperature ($T_{\text{H,local}}$) and the local cold reservoir temperature ($T_{\text{C,local}}$), as expressed in Equation (12). It's worthy to mention that when the temperature of the heat reservoir ($T_{\text{H,end}}$) equals the temperature of the cold reservoir ($T_{\text{C,end}}$), the energy conversion process reaches the upper limit.

$$\eta_{therm,global} = 1 - \frac{T_{C,ave}}{T_{H,ave}} \tag{11}$$

$$\eta_{therm,global} = 1 - \frac{T_{C,local}}{T_{H,local}} \tag{12}$$

According to the definition of entropy,[45] $T_{\text{H,ave}}$ and $T_{\text{C,ave}}$ can be expressed as:

$$T_{H,ave} = \frac{\int_{s_{H,ini}}^{s_{H,end}} T_H ds_H}{s_{H,end} - s_{H,ini}} \tag{13}$$

$$T_{C,ave} = \frac{\int_{s_{C,ini}}^{s_{C,end}} T_C ds_C}{s_{C,end} - s_{C,ini}} \tag{14}$$

where s_H and s_C are the specific entropy of heat reservoir and cold reservoir respectively; $s_{\text{H,end}}$ and $s_{\text{H,ini}}$ refer to the specific entropy of the heat reservoir at the ending state and initial state, respectively; $s_{\text{C,end}}$ and $s_{\text{C,ini}}$ refer to the specific entropy of the cold reservoir at the ending state and initial state, respectively; Moreover, according to the Clausius inequality,[45] for a reversible process, the total entropy variation of the system (dS_{system}) during energy conversion process is 0. Therefore, based on this characteristic, the energy distribution of the system at any moment can be calculated.

Through the above mathematical description, the energy distribution of the system on the E_T-E_M diagram can be determined, as shown in Figure 1B. According to the 2nd Law of Thermodynamic, there is an upper limit of energy conversion when thermal energy is converted into mechanical energy, that is, the Carnot cycle. Therefore, the thermal energy within the system cannot be fully converted into mechanical energy. Moreover, in the heat-work conversion process, there is only energy transfer between the heat reservoir and cold reservoir without any mass exchange, where the enthalpy of the ideal gas variation continually within the heat reservoir and cold reservoir, corresponding in the change of reservoir temperature. As a result, the temperature difference between two reservoirs continuously varies, leading to the local thermal efficiency ($\eta_{\text{Carnot,local}}$) change accordingly. To more comprehensively describe the efficiency variations during the heat-work conversion process, the variation of energy in heat reservoir with the increasing mechanical energy is adding in the E_T-E_M diagram, as shown by the blue curve in Figure 3C. For any point on the curve, the slope (k) is equal to the ratio of the reduction in heat reservoir ($\Delta E_{\text{H,local}}$) to the increase in mechanical energy ($\Delta E_{\text{M,local}}$), both of which are the parameters of consisting $\eta_{\text{therm,local}}$. Therefore, $\eta_{\text{therm,local}}$ can be represented by the geometry parameters on the E-E diagram, which can revised from Equation (12)-(15).

$$\eta_{therm,local} = -\frac{1}{k} \tag{15}$$

Another noteworthy characteristic in the curve is that the vertical and horizontal distances between the start and end points represent the variation in the heat reservoir capacity ($\Delta E_{\text{H,global}}$) and the increase in mechanical energy ($\Delta E_{\text{M,global}}$), respectively. The ratio of these two distances constitutes the global thermal efficiency ($\eta_{\text{therm,global}}$). According to trigonometric relationships, this value precisely corresponds to the tangent of the angle ω. Therefore, $\eta_{\text{therm,global}}$ can also be expressed using the geometric parameters on the E-E diagram, as shown in Equation (16).

$$\eta_{therm,global} = \tan\omega \tag{16}$$

In actual heat-work conversion process, the inevitable of irreversible phenomena within the system results in the deviation of global thermal efficiency ($\eta_{\text{global,actual}}$) from the ideal working condition, as shown in Figure 1D. Moreover, the ratio of these two efficiencies is commonly referred to as the thermodynamic perfection degree ($\varepsilon_{\text{per,global}}$), as expressed in Equation (17). However, in actual working conditions, due to the irreversible losses, a greater portion of the thermal energy from heat reservoir transfer into the cold reservoir without being converted into work, resulting in different ending temperatures. Consequently, in these two working conditions, not only the conversion mechanical energy is different, but also the total heat transfer from heat reservoir is different.

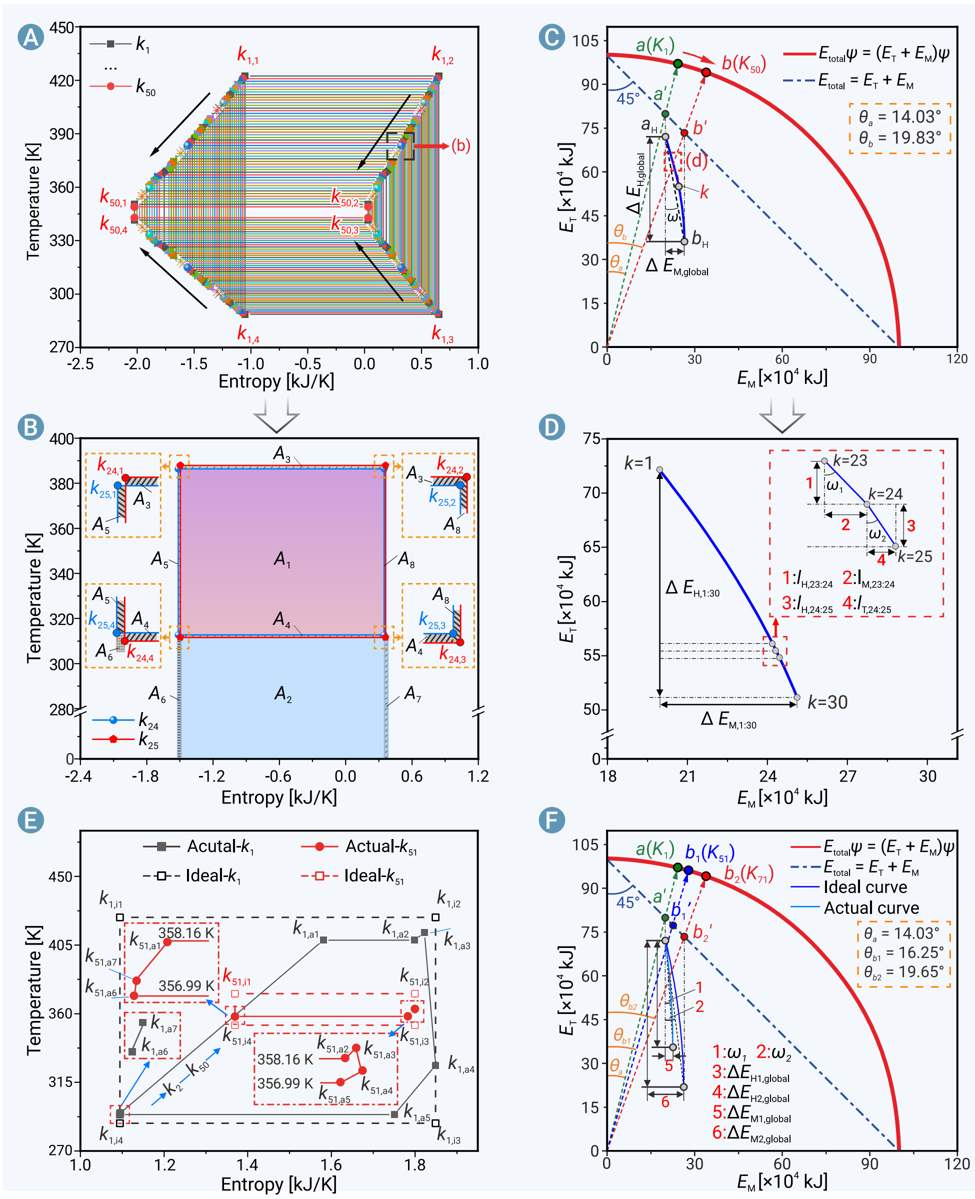

Figure 3. Graphical comparison between *T-s* diagram and *E-E* diagram. Ideal working conditions *T-s* diagram of the (A) whole conversion process and (B) process step 24 and 25; *E-E* diagram of the (C) whole conversion process and (D) process step 24 and 25; Actual working conditions: (E) *T-s* diagram and (F) *E-E* diagram.

In summary, the construction of the E_T-E_M diagram can be summarized as three steps:

1. Representation of system total energy (Red arc): Draw a red arc with the origin (O) at (0,0) and a radius (r) equal to the total energy (E_{total});

2. Representation of initial system point (Point a): Determine point a' (E_M,E_T) based on the initial energy distribution. Connect Oa' and extend the line to intersect the red arc, identifying the intersection as point a.

3. Representation of heat reservoir capacity variation and mechanical energy variation (Blue curve): Determine the energy distribution variation during heat-work conversion process using Equations (6)-(14). Draw the curve representing the variation in heat reservoir capacity with the increase in mechanical energy, and identify the ending point as point b_i.

Through above three steps, the distribution of system energy on the E-E diagram can be determined. Subsequently, the system's performance parameters can be derived from the geometric parameters. The E-E diagram represents not only the system parameters related to the 1st and 2nd Laws of Thermodynamics, but also the global and local parameters under dynamic boundary conditions.

$$\varepsilon_{\mathrm{per,global}} = \frac{\tan \omega_b}{\tan \omega_c} \tag{17}$$

where the subscription b, c represents the end point under actual working condition and ideal working conditions respectively. For local thermodynamic perfection degree ($\varepsilon_{\mathrm{per,local}}$), it is defined as the ratio of the local thermal efficiency between the actual working conditions ($\eta_{\mathrm{actual,local}}$) and ideal working conditions ($\eta_{\mathrm{ideal,local}}$) under the same heat source capacity. According to Equation (16), $\varepsilon_{\mathrm{per,local}}$ is the ratio of the slopes, as shown in Equation (18).

$$\varepsilon_{\mathrm{per,local}} = \frac{k_{ideal}}{k_{actual}} \tag{18}$$

where k_{ideal} and k_{actual} are the slope under ideal working conditions and actual working conditions respectively. Besides $\varepsilon_{\mathrm{per,global}}$, global exergy efficiency ($\varepsilon_{\mathrm{ex,global}}$) is also a commonly used indicator to evaluate the deviation of the actual thermomechanical conversion process from ideal conditions, which is defined as the ratio of the increase in mechanical energy under actual working conditions to ideal working conditions. Since the initial points of the system are the same under both conditions, the exergy efficiency can be revised into Equation (19) by referencing Equation (5).

$$\varepsilon_{\mathrm{ex,global}} = \frac{1 - \frac{1+\tan\theta_a}{1+\tan\theta_b}}{1 - \frac{1+\tan\theta_a}{1+\tan\theta_c}} \tag{19}$$

where the subscription a represents the initial point.

RESULTS AND DISCUSSION

Boundary conditions in graphical method comparison. To intuitively observe the graphical differences between the E-E diagram and the T-s diagram, the Carnot cycle and an actual cycle under a finite heat capacity boundary capacity are selected as case studies to analysis. The geometry parameters of system performance in the diagram are compared. In isolated system, the system contains 8×10^5 kJ of thermal energy (E_T) and 2×10^5 kJ of mechanical energy (E_M). Moreover, E_T consists of a heat reservoir (E_H) with a capacity of 4×10^5 kJ at an initial temperature of 423.15 K and a cold reservoir (E_C) with a capacity of 4×10^5 kJ at an initial temperature of 288.15 K. Under ideal working conditions, the working fluid that facilitate the heat-work conversion between the thermal reservoir and the mechanical energy reservoir is an ideal gas. The thermodynamic processes of Carnot cycle include isothermal heat absorption, adiabatic expansion, isothermal heat release, and adiabatic compression, with no irreversible losses in the heat-work conversion process. To simplify the calculation process, a process step size of 0.1% of the thermal reservoir's capacity (ΔE_H = 0.1% E_H) is assumed, during which the temperatures of the heat or cold reservoirs remain constant. For the next step, the reservoir temperature is update through the energy conversion efficiency of the last step until the temperature difference between the heat and cold reservoirs equalizes. To ensure the accuracy of the calculation results, a comparison was made with the theoretical results proposed by Ma et al.[46] Details of the comparison results are provided in the ***Supplemental Information***.

Under actual working conditions, irreversible losses occur during the heat-work conversion process. Taking an organic Rankine cycle (ORC) as an example, the temperature difference during the heat exchange between the working fluid and the heat or cold reservoirs and the friction loss during

Table 1. Comparison between the *E-E* diagram and the *T-s* diagram

Items	*E-E* diagram	*T-s* diagram
Description object	Energy reservoir	Working fluid
System performance variation	Intuitively	Non-intuitively
Working fluid state	Non-intuitively	Intuitively
Graphic geometry parameters	Angle (θ and ω), Line (l) and slope (k)	Area (A)
Global system performance		
Thermal efficiency ($\eta_{therm,global}$)	$\tan\omega$	$\frac{\sum A_{work}}{\sum A_{absorption}}$
Exergy efficiency ($\varepsilon_{ex,global}$)	$\frac{1-\frac{1+\tan\theta_a}{1+\tan\theta_b}}{1-\frac{1+\tan\theta_a}{1+\tan\theta_c}}$	$\frac{\sum A_{work,actual}}{\sum A_{work,ideal}}$
Thermodynamic perfection degree ($\varepsilon_{per,global}$)	$\frac{\tan\omega_b}{\tan\omega_c}$	$\frac{\sum A_{work,actual}\sum A_{absorption,ideal}}{\sum A_{absorption,actual}\sum A_{work,ideal}}$
Local system performance		
Thermal efficiency ($\eta_{therm,local}$)	$-\frac{1}{k}$	$\frac{A_{work,i}}{A_{absorption,i}}$
Thermodynamic perfection degree ($\varepsilon_{per,local}$)	$\frac{k_{ideal}}{k_{actual}}$	$\frac{A_{work,actual}A_{absorption,ideal}}{A_{absorption,actual}A_{work,ideal}}$

Table 2. Initial boundary conditions

Case	$E_{T,ini}/E_{M,ini}$ (×10^5 kJ)	$E_{H,ini}/E_{C,ini}$ (×10^5 kJ)	$T_{H,ini}/T_{C,ini}$ (K)	m_H (kg)	m_C (kg)
1	80:20	40:40	**500/300**	33.93	286.70
2	80:20	40:40	**1000/300**	10.59	286.70
3	80:20	40:40	**1500/300**	6.27	286.70
4	80:20	**72:8**	1000/300	19.06	57.34
5	80:20	**8:72**	1000/300	2.12	516.51

expansion or compression processes lead to the irreversible phenomenon, which decreases the energy conversion efficiency, causing the system's performance to deviate from the ideal working conditions. The details of ORC can be seen in ***Supplemental Information***. To demonstrate the variation in the system performance, a time step size of 100 s is set, during which the temperatures of the heat or cold reservoir remain constant. The reservoir temperature in the next time step is also adjusted based on the result of last time step.

Ideal working conditions comparison. As the heat-work conversion process progresses, part of the thermal energy in the heat reservoir is continuously converted into mechanical energy, while the remaining thermal energy is transferred into the cold reservoir, until the energy conversion efficiency reaches its upper limit. Figure 3 depicts the system performance in the *T-s* and *E-E* diagrams under finite heat capacity working conditions. As the process step (k_{50}) is 50, the temperature difference between the heat reservoir and the cold reservoir is less than 10 K, which represents that the system has reached the upper limit of conversion efficiency.

In the *T-s* diagram (Figure 3A), the working fluid undergoes heat absorption process ($k_{i,1}$-$k_{i,2}$, where i represents the process step), expansion process ($k_{i,2}$-$k_{i,3}$), heat releasing process ($k_{i,3}$-$k_{i,4}$), and compression process ($k_{i,4}$-$k_{i,1}$) during each process step. It can be easily observed that each thermodynamic process in *T-s* diagram appears as a straight line, and the enclosed rectangular area of four process represents the net conversion mechanical energy ($\Delta E_{M,i}$) during one step. Since the heat and cold reservoir temperatures do not keep as a constant throughout the conversion process, the thermodynamic state points vary in each step, leading to changes in the rectangular area. Consequently, when all the state point variations are plotted on the same *T-s* diagram, the graph becomes non-intuitively, making it difficult to analyze system performance. Moreover, for any two adjacent process steps, the variation in the system performance cannot be intuitively observed. For instance, in step 24th (k_{24}) and 25th (k_{25}), the overlapping area of net conversion mechanical energy ($\Delta E_{M,i}$) and heat absorption ($\Delta E_{H,i}$) are A_1 and (A_1+A_2) respectively, as shown in Figure 3B. In k_{24}, $\Delta E_{M,24}$ and $\Delta E_{H,24}$ is equals to (A_1+ A_3+ A_4+ A_8) and (A_1+ A_2+ A_3+ A_4+ A_7+ A_8) respectively, with the thermal efficiency ($\eta_{local,24}$) being the ratio of these two areas. When the process progresses to k_{25}, $\Delta E_{M,25}$ and $\Delta E_{H,25}$ is equals to (A_1+ A_5) and (A_1+ A_2+ A_4+ A_5+ A_6) respectively, where comparing the thermal efficiency ($\eta_{local,25}$) and $\eta_{local,24}$ intuitively through the *T-s* diagram is challenging.

When the system performance graphics on the *E-E* diagram (Figure 3C), it can be observed that the efficiency change caused by the temperature difference variation between the heat reservoir and cold reservoir is reflected in the slope (k) change of the heat source capacity curve, and the accumulated conversion mechanical energy ($\sum_{i=1}^{n}\Delta E_{M,i}$) during the entire process is represented by the change in angle θ. In k_{24}, $\Delta E_{M,24}$ and $\Delta E_{H,24}$ is represented by the lines $l_{M,23:24}$ and $l_{H,23:24}$, respectively, and the corresponding local thermal efficiency is $\tan\omega_1$, as depicted in Figure 3D. Similarly, in k_{25}, $\Delta E_{M,25}$ and $\Delta E_{H,25}$ is represented by the line $l_{M,24:25}$ and $l_{H,24:25}$, and the corresponding local thermal efficiency is $\tan\omega_2$. As $\tan\omega$ is a monotonically increasing function in the interval [0, 90°], a smaller ω indicates a lower η_{local}. Furthermore, as the system transitions from the initial state to the final state, θ rotates from 14.03° to 19.83°. According to Eq. (2), $\sum_{i=1}^{50}\Delta E_{M,i}$ is 9.67×10^3 kJ. Compared to the *T-s* diagram, comparing the angles is more intuitive than comparing two area ratios, which is the advantage of the *E-E* diagram.

Actual working conditions comparison. In the heat-work conversion process under actual working conditions, the design of a thermodynamic system is commonly constrained by mechanical components and investment costs, which necessitates accounting for the phase change of the working fluid during the heat transfer process and temperature differences

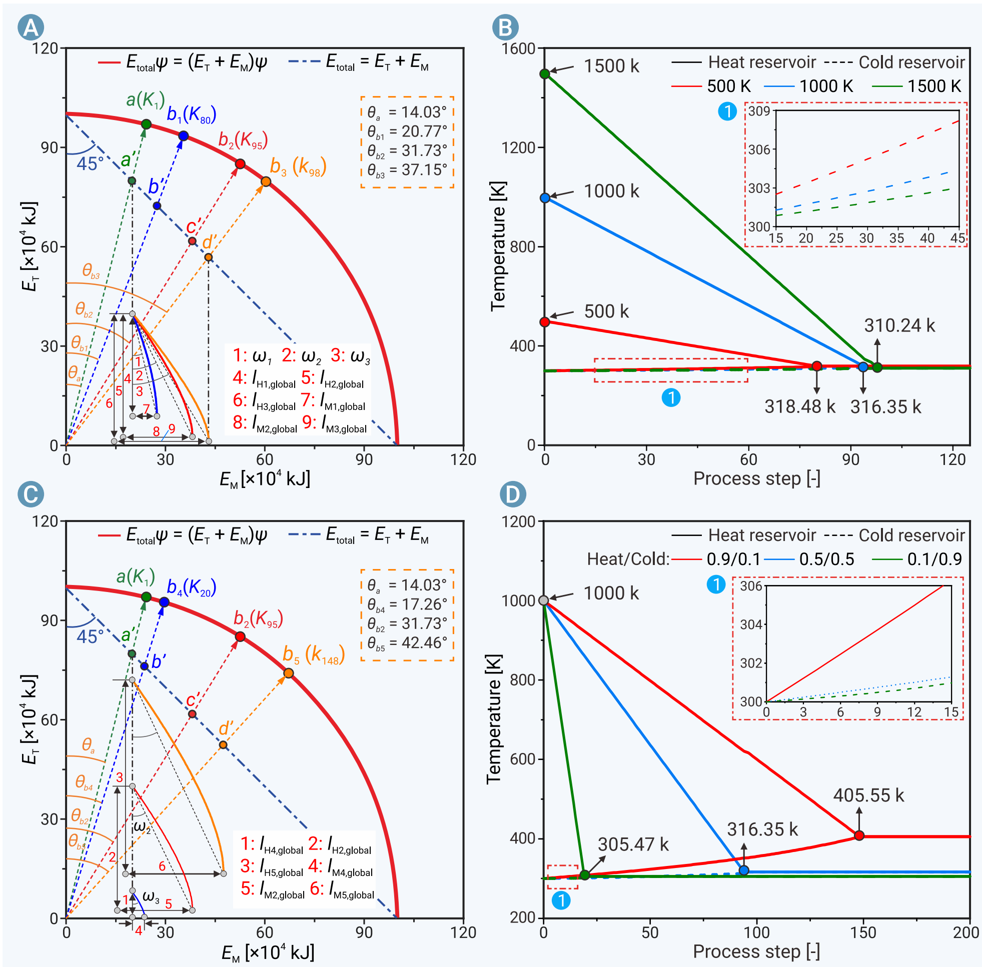

Figure 4. Graphical representation under different working conditions Initial heat reservoir temperature (A) *E-E* diagram and (B) Temperature variation; Initial energy distribution: (C) *E-E* diagram and (D) Temperature variation.

between the working fluid and heat/cold reservoir. These factors result in more complex thermodynamic processes. Moreover, the irreversible phenomenon causes entropy changes in the working fluid during compression/expansion processes, leading to the transformation of the enclosed area in the *T-s* diagram from a rectangle under ideal working conditions into a complex irregular shape (Figure 3E). It can also be observed that as the energy conversion process progresses, the enclosed area of ORC in the *T-s* diagram continues to shrink. Correspondingly, the area of the ideal cycle also decreases. Since the ratio of these two areas represents the degree to which the actual cycle deviates from the ideal cycle, i.e., the local thermodynamic perfection degree ($\eta_{per,local}$), it becomes easy to analyze the irreversible losses of each thermodynamic process under steady-state conditions. However, under dynamic boundary conditions, due to the continuous change in area, not only is the variation trend of thermal efficiency difficult to observe intuitively, but the trend of thermodynamic perfection is also not easily visualized.

In the *E-E* diagram (Figure 3F), when the system reaches the upper limit of energy conversion under actual conditions, the radius rotates from point a (θ_a = 14.03°) to point b_1 (θ_{b1} = 16.25°), while under ideal conditions, the absence of irreversible factors results in more converted mechanical energy, and the corresponding radius rotation reaches point b_2 (θ_{b2} = 19.65°). According to Eq. (19), the global exergy efficiency ($\varepsilon_{global,ex}$) of the system can be calculated through these three angles, which is 40.81%. Additionally, in the heat reservoir capacity curve (two blue curves), the angle (ω_1) between the line connecting the starting (a_H) and ending points (b_{H1}) of the actual operating curve and the vertical direction is significantly lower than that of the ideal case (ω_2), which indicates a lower global thermal efficiency. Limited by the temperatures of the heat and cold reservoirs, the heat released from the heat reservoir under actual conditions ($\Delta E_{H1,global}$) and under ideal conditions ($\Delta E_{H2,global}$) also differs, being 36.72 kJ and 50.40 kJ, respectively. Correspondingly, the conversion mechanical energy under actual conditions ($\Delta E_{M1,global}$) and under ideal conditions ($\Delta E_{M2,global}$) also varies, amounting to 2.58 kJ and 6.32 kJ, respectively. In addition to global performance parameters, by observing the heat reservoir capacity curves, it can also be noted that within the same process step (where the heat reservoir capacity is the same), the slope of the curve under actual conditions is steeper than that under ideal conditions. According to Eq. (15), the local thermal efficiency ($\eta_{therm,local}$) under actual conditions is lower than that under ideal conditions, with the ratio of the two representing the local thermodynamic perfection degree ($\varepsilon_{per,local}$). Interestingly, it's worthy to mentioned that the horizontal distance ($l_{ex,loss}$) between the two curves represents the difference in accumulated converted mechanical energy ($\sum \Delta E_{M,loss}$). In summary, the *E-E* diagram has the advantage on describing system performance variations under dynamic boundary conditions.

Remarks. The *E-E* diagram has advantages over the *T-s* diagram in describing system performance under dynamic boundary conditions, which can be attributed to the difference in description object. The differences between the two graphical analysis methods are shown in Table 1. For the *E-E* diagram, it describes the system performance from the perspective of reservoirs and is not limited to the energy conversion medium, which allows for the performance description between difference heat-work conversion devices. The geometric parameters used to describe system performance are line length (l) and angle (θ and ω), with changes in the curve slope (k) representing the variation in system performance, thereby enabling a comprehensive description of system performance under dynamic boundary conditions. On the other hand, the *T-s* diagram explicitly focuses on the medium of energy conversion and describes the thermodynamic cycle from the perspective of the working fluid. The thermodynamic state changes of the working fluid during a thermodynamic cycle can be fully represented, and the geometric parameter used to describe system performance is area. Under fixed boundary conditions, the areas corresponding to heat and work exchanges remain constant, and by analyzing the differences between ideal and actual processes, the system's thermodynamic performance can be evaluated.

For an energy conversion process under dynamic boundary conditions, the thermodynamic state graphical method (*T-s* diagram, *P-v* diagram and so on.) shows the system performance deviation between actual working conditions and ideal working conditions at each moment, while the thermodynamic process graphical method shows the deviation for entire conversion process. A synergy analysis of two methods is expected to provide a more comprehensive understanding of system performance and state changes, offering a new perspective for the design of thermodynamic systems.

Boundary conditions in Graphical representation under varying initial state. The *E-E* diagram method enriches the description of system performance parameters under dynamic boundary conditions. To gain a deeper understanding of the characteristics of geometric parameters in the *E-E* diagram under different initial boundary conditions, several cases under ideal working conditions were conducted on the heat-work conversion process under varying initial cold/heat reservoir temperatures (Cases 1–3) and initial energy distributions (Cases 2, 4 and 5). The initial boundary conditions are shown in Table 2. It is worth noting that, under the same energy distribution, the enthalpy of the ideal gas in the heat reservoir (h_H) differs due to the varying

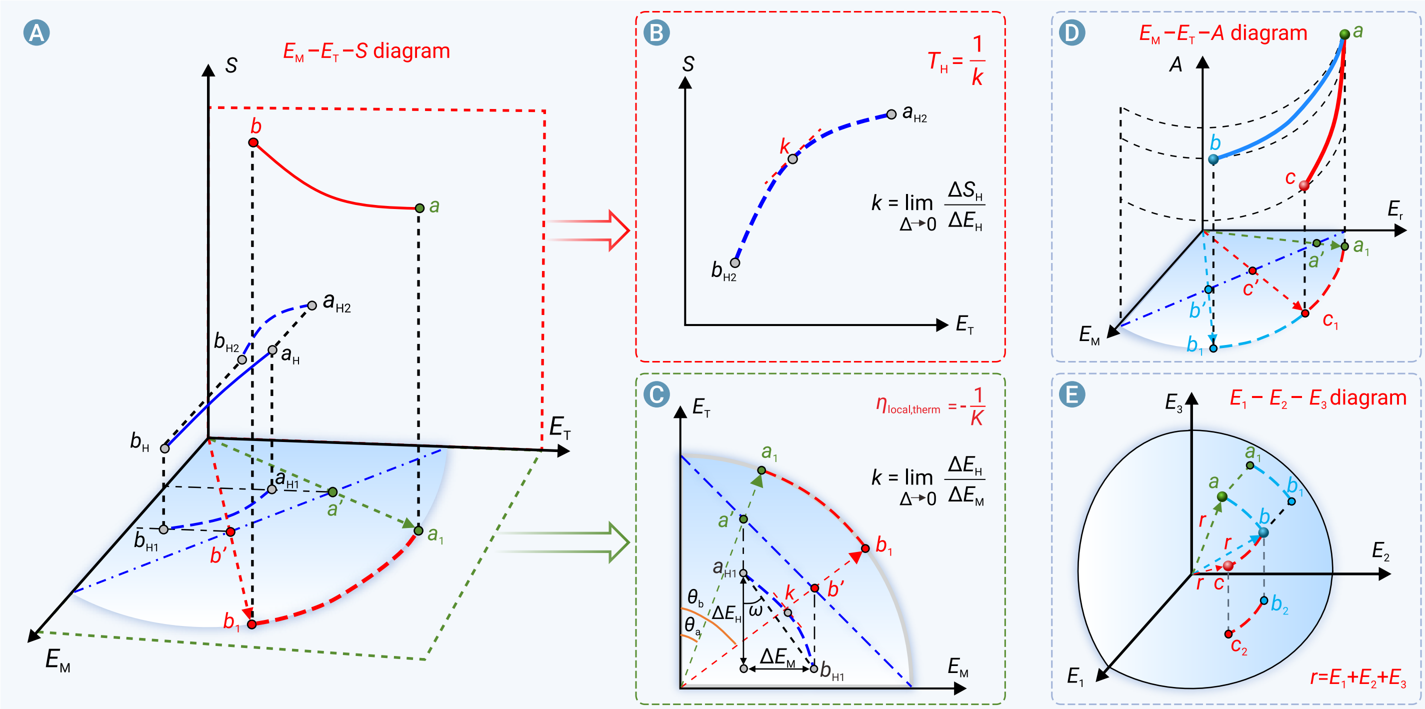

Figure 6. Extension of *E-E* diagram (A) E_M-E_T-S diagram, (B) E_T-S diagram, (C) E_M-E_T diagram, (D) E_M-E_T-A diagram and (E) E_1-E_2-E_3 diagram.

initial temperatures of the heat reservoir, and accordingly, the mass (m_H) also varies, showing an inverse relationship with the trend of h_H.

Initial heat reservoir temperature. At different initial heat reservoir temperatures ($T_{H,ini}$), the graphical parameters of each case in the *E-E* diagram exhibit significant differences, as shown in Figure 4A. At the initial state, since the distributions of thermal energy and mechanical energy are consistent, the angle at the initial state point *a* (θ_a) of three cases are all equal to 14.03°. As the heat-work conversion process progresses, the radius gradually rotates along the red arc to point *b*, and the angle (θ_b) increases from 20.77° at $T_{H,ini}$ of 500 K to 37.15° at 1500 K, indicating that more converted mechanical energy (ΔE_M) can be obtained. In the curve of heat reservoir capacity changes, it can also be observed that with higher initial temperatures, the angle (ω) between the starting and ending points of the curve and the y-axis increases, which indicates that the system has a higher global thermal efficiency at these temperatures. Furthermore, the graphical parameters on the *E-E* diagram allow us to examine the impact of $T_{H,ini}$ on the heat release from the heat reservoir. When $T_{H,ini}$ is 500 K, the corresponding line length for the heat release from the heat reservoir is $l_{H1,global}$, which is significantly lower than $l_{H2,global}$ at 1000 K and $l_{H3,global}$ at 1500 K. The phenomenon can be attributed to the temperature variation regulation of the two thermal reservoirs. As $T_{H,ini}$ increases, the initial local thermal efficiency ($\eta_{therm,1}$) also rises, resulting in the less heat transferring to the cold reservoir for the same heat release amount from the heat reservoir. Consequently, the temperature increase of the local cold reservoir becomes smaller, while the greater temperature difference between the heat and cold reservoirs leads to a larger total heat release from the thermal reservoir throughout the energy conversion process.

Due to the varying local thermal efficiencies ($\eta_{therm,local}$) along the process, the temperature changes in the thermal and cold reservoirs are closely related to $T_{H,ini}$, as shown in Figure 4B. As $T_{H,ini}$ increases, the number of process steps experienced during the heat-work conversion process rises from 80 at 500 K to 98 at 1500 K, indicating an increase in the thermal reservoir capacity change (ΔE_T). Correspondingly, the ending temperature (T_{end}) after reaching the upper limit of heat-work conversion gradually decreases from 318.48 K to 310.24 K. Meanwhile, a lower initial thermal reservoir temperature results in more heat released to the cold reservoir during the same process step, leading to a higher temperature rise in the cold reservoir. Consequently, at lower heat reservoir temperatures and higher cold reservoir temperatures, the slope (k) of the heat reservoir capacity curve in the *E-E* diagram will be lower, reflecting a decreased $\eta_{therm,local}$. Additionally, at the same $T_{H,ini}$, as the heat-work conversion process progresses, the continuously decreasing temperature difference between the heat and cold reservoirs causes k to decrease with increasing mechanical energy, resulting in a continual decline in $\eta_{therm,local}$.

Initial energy distribution. When the initial distribution of thermal energy varies, the upper limit of energy conversion that the system can achieve also differs. Figure 5C shows the system performance variations under different initial energy distributions. The results indicate that, with a fixed total amount of thermal energy, the angle (θ) through which the radius rotates increases from 17.26° (θ_{b4}) at a heat reservoir to cold reservoir capacity ratio of 10%/90% to 42.46° at a ratio of 90%/10%. However, in the thermal capacity change curve, the trend of global thermal efficiency ($\eta_{therm,global}$) exhibits the opposite behavior; as the initial heat reservoir capacity increases, ω decreases from 27.93° to 25.15°, indicating a slight reduction in $\eta_{therm,global}$. This phenomenon is primarily caused by temperature changes during the heat-work conversion process, as illustrated in Figure 5D. Within the same process step, a higher heat reservoir capacity ratio leads to a greater mass of ideal gas in the heat reservoir, resulting in less temperature variation. Simultaneously, the mass of the ideal gas in the cold reservoir decreases, causing a larger temperature change in the cold reservoir. However, since the heat absorption in the cold reservoir is significantly lower than the heat release in the heat reservoir, the rate of temperature change in the cold reservoir is much lower than that in the thermal reservoir, which shows a larger temperature difference between the two reservoirs, leading to higher thermal efficiency. Furthermore, due to the higher heat reservoir capacity ratio, the total heat released by the heat reservoir also shows a significant increase, with its ending temperature rising from 305.47 K to 405.55 K. Consequently, under the interaction of these factors, the system's global thermal efficiency exhibits a slight downward trend.

Current status and limitations of *E-E* diagram. In this section, the advantages, limitations, and applicability of the *E-E* diagram will be reviewed and prospected. As mentioned in previous sections, the graphical analysis method based on thermodynamic process parameters has the advantage of representing changes in system performance through the variations in angles, without being limited to a single heat-work conversion device or a single working fluid. However, the *E-E* diagram struggles to reflect changes in

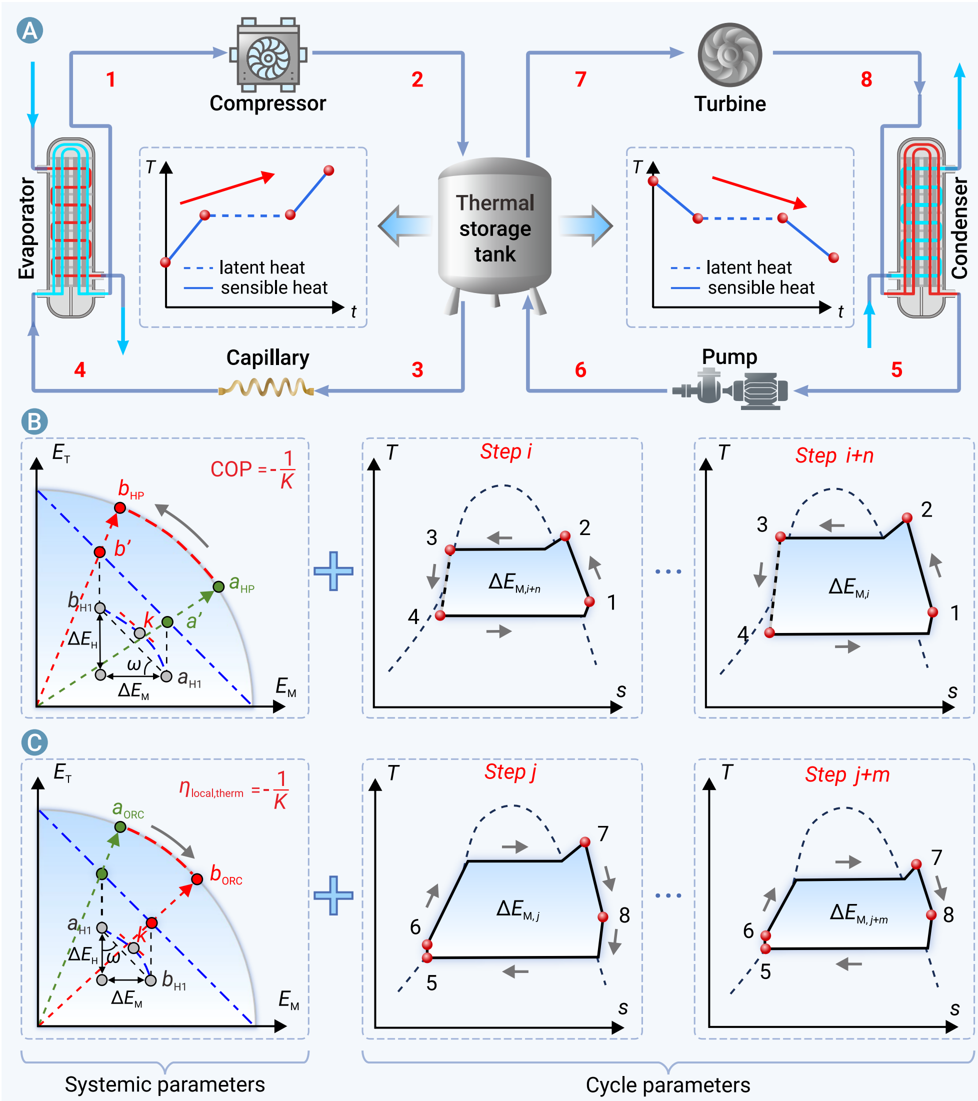

Figure 5. Potential application of *E-E* diagram (A) Schematic of Carnot battery system (CB), (B) Graphical representation of heat pump sub-system (HP), (C) Graphical representation of organic Rankine cycle sub-system (ORC).

the temperature of the heat reservoir during the heat-work conversion process, necessitating a combined analysis with other graphical methods. The extension of *E-E* graphical method is crucial for advancing the analysis of system performance in energy conversion processes under dynamic boundary conditions.

Potential applications of *E-E* diagram. With the integration of renewable energy and thermal energy storage technologies into thermodynamic systems, the finite storage capacity introduces dynamic boundary conditions during thermal energy storage and release processes. This leads to continuous variations in local thermal efficiency of ideal cycles, which differs significantly from traditional coal-fired power plants where heat reservoir was considered to have infinite thermal capacity due to continuous coal combustion. Therefore, the design of novel thermodynamic systems requires consideration of dynamic transformation characteristics.

The Carnot Battery (CB), a recently proposed novel energy storage system,[47] serves as an illustrative example. As shown in Figure 5A, it comprises a heat pump (HP) subsystem and an organic Rankine cycle (ORC) subsystem. The phase change material (PCM) in the system undergoes three stages during heat storage and release: initial sensible heat, latent heat, and final sensible heat. As the heat exchange between the HP condenser (process 4-1) and ORC evaporator (process 8-5) causes temperature variations in the thermal storage tank, the operating states of both HP and ORC continuously evolve during CB operation. As shown in Figures 5B & C, the combined analysis using the *E-E* and the *T-s* diagrams allows for comprehensive system performance evaluation. The *E-E* diagram reveals both global and local performance parameters, while the *T-s* diagram enables detailed analysis of working fluid states at specific operating points (step *i*, step *i+n*, step *j* and step *j+m*), such as the impact of pinch point variations during the transition from sensible to latent heat storage. This combined-analysis approach enhances our understanding of CB system operational characteristics and can be similarly applied to other scenarios involving finite heat capacity systems.

Extension of *E-E* diagram. According to the 2nd Law of Thermodynamics, the total entropy of an isolated system (ΔS_{iso}) during the energy conversion process exhibits unidirectionality. If the energy form in the conversion process is abstracted as an isolated system, the *E-E* diagram can be more powerful by incorporating the state parameter of entropy, thus constructing a three-dimensional graphical analysis method that couples process quantities and state quantities (E_M-E_T-S), as shown in Figure 6A. This method allows for a comprehensive description of the along-the-way evolution of ΔS_{iso} during the energy conversion process, enabling the evaluation of irreversible losses. Additionally, according to the definition of Clausius entropy, the ratio of heat change (ΔE_H) to entropy change (ΔS_H) represents temperature, while the slope of the heat capacity curve (k) projected on the S-E_T diagram (Figure 6B) precisely indicates the inverse of the thermal reservoir temperature (T_H); the higher k represents the lower T_H. These two advantages can further enhance the description of energy conversion processes under dynamic boundary conditions.

In fact, beyond the *E-E-S* diagram, the third-dimensional coordinate can be adjusted based on the application scenario and analytical objectives. For example, when assessing the energy level change during the energy conversion process, we can add an energy quality evaluation index (A)[48-51] for a more comprehensive analysis, as depicted in Figure 6C. By illustrating the along-the-way evolution of energy quality in the energy conversion process, we can select different energy conversion paths to minimize energy quality loss. Similarly, when the energy conversion process involves multiple forms of energy, the third-dimensional coordinate can be extended to the third energy forms (E_3), transforming the original red arc into a three-dimensional sphere, as shown in Figure 6E. The length of the sphere's radius (r) still represents the total energy of system, and the rotation of radius on the sphere in the radius does not affect the length of radius, thus achieving the representation of the first law of thermodynamics. Moreover, by describing the trajectory changes of system state points on this sphere, a comprehensive description of energy changes during the conversion process can be achieved.

CONCLUSION

Based on the perspective of energy distribution, the *E-E* diagram characterizes energy conversion processes through its geometric features. The innovation of the *E-E* diagram lies in two keys: first, it represents the 1st Law of Thermodynamics by analogizing the energy conversion process to the rotational motion of a radius in a circle; second, it illustrates the 2nd Law of Thermodynamics through the rotation angle (θ) of the radius. Additionally, the geometric parameters (ω, k and l) in the E-E diagram effectively describe both global and local system performance. Compared to the T-s diagram, the E-E diagram not only provides a more intuitive visualization of system performance variations but also offers a broader applicability due to its independence from specific heat-work conversion devices or working fluids. The coupling of process quantities and state variables in this graphical analysis method shows promising potential for describing system performance and state variations in energy conversion processes. Furthermore, the addition of energy level (A) or the third form of energy (E_3) as a third dimension in the E-E diagram offers a novel perspective for describing energy quality changes and multi-energy conversion processes, which could offer new insights into the optimization of renewable energy conversion pathways.

REFERENCES

1. Song H., Wang H., Zheng H., et al. (2023). Analysis of cascade and hybrid processes for hydrogen production by full spectrum solar energy utilization. *Energy Conv. Manag.* **291**:117289. DOI:10.1016/j.enconman.2023.117289
2. Liang Z., Liang Y., Luo X., et al. (2024). Multi-objective optimization of proton exchange membrane fuel cell based methanol-solar-to-X hybrid energy systems. *Appl. Energy* **373**:123828. DOI:10.1016/j.apenergy.2024.123828
3. Jiao K., Xuan J., Du Q., et al. (2021). Designing the next generation of proton-exchange membrane fuel cells. *Nature* **595**:361–369. DOI:10.1038/s41586-021-03482-7
4. Yan H., Zhang C., Shao Z., et al. (2023). The Underestimated Role of the Heat Pump in Achieving China's Goal of Carbon Neutrality by 2060. *Engineering* **23**:13–18. DOI:10.1016/j.eng.2022.08.015
5. Yan H., Ahrens M.U., Hertwich E., et al. (2024). Heat pumps as a sustainable bridge for global heating and cooling at multi-scale. *Energy Environ. Sci.* **17**:2081–2087. DOI:10.1039/d3ee04246d
6. Tang W., Xu S., Zhou X., et al. (2023). Meeting China's electricity demand with renewable energy over Tibetan Plateau. *Sci. Bull.* **68**:39–42. DOI:10.1016/j.scib.2022.12.012
7. Jiao F., Chen C., Liu T., et al. (2024). Insights of water-to-hydrogen conversion from thermodynamics. *Innov. Energy* **1**:100004. DOI:10.59717/j.xinn-ener.2024.100004
8. Liang H., Rehan M.A., Li J., et al. (2024). Kinetic simulation of hydrogen production reaction parameters based on TiO2 photocatalyst. *Appl. Therm. Eng.* **239**:122134. DOI:10.1016/j.applthermaleng.2023.122134
9. Liu H., Yu M., Tong X., et al. (2024). High Temperature Solid Oxide Electrolysis for Green Hydrogen Production. *Chem. Rev.* **124**:10509–10576. DOI:10.1021/acs.chemrev.3c00795
10. Chen R., Xu W., Deng S., et al. (2022). Energy quality and energy grade: concepts, applications and prospects. *Oxford Open Energy* **1**:oiac001. DOI:10.1093/ooenergy/oiac001
11. Lin M., Suter C., Diethelm S., et al. (2022). Integrated solar-driven high-temperature electrolysis operating with concentrated irradiation. *Joule* **6**:2102–2121. DOI:10.1016/j.joule.2022.07.013
12. Wang Y., Zhang L., Song Y., et al. (2024). State-of-the-art review on evaluation indicators of integrated intelligent energy from different perspectives. *Renew. Sust. Energy Rev.* **189**:113835. DOI:10.1016/j.rser.2023.113835
13. Wallington T.J., Woody M., Lewis G.M., et al. (2024). Green hydrogen pathways, energy efficiencies, and intensities for ground, air, and marine transportation. *Joule* **8**:2190–2207. DOI:10.1016/j.joule.2024.07.012
14. Huang Y., Chen J., Chen Y., et al. (2022). Performance explorations of an organic Rankine cycle featured with separating and mixing composition of zeotropic mixture. *Energy* **257**:124535. DOI:10.1016/j.energy.2022.124535
15. Liang Y., Guo Z., Luo X., et al. (2024). An adaptive CO2 Brayton-Rankine power cycle for efficient utilization of low environment temperature: A thermodynamic analysis and optimization study. *J. Clean. Prod.* **435**:140547. DOI:10.1016/j.jclepro.2023.140547
16. Huang Y., Chen J., Chen Y., et al. (2023). Performance explorations of a novel high temperature heat pump with multi-adjusted compositions of zeotropic mixture. *Appl. Therm. Eng.* **235**:121409. DOI:10.1016/j.applthermaleng.2023.121409
17. Chen J., Yang N., Li J., et al. (2024). Evaluations of heat pump water heater with liquid-separation condensation from perspectives of performance enhancement and heat exchange area reduction. *Int. J. Refrig.* **161**:21–30. DOI:10.1016/j.ijrefrig.2024.02.026
18. Akbar N.S., Rafiq M., Muhammad T., et al. (2024). Microbic flow analysis of nano fluid with chemical reaction in microchannel with flexural walls under the effects of thermophoretic diffusion. *Sci. Rep.* **14**:50915. DOI:10.1038/s41598-023-50915-6
19. Akbar N.S., Rafiq M., Muhammad T., et al. (2024). Electro osmotically interactive biological study of thermally stratified micropolar nanofluid flow for Copper and Silver nanoparticles in a microchannel. *Sci. Rep.* **14**:51017. DOI:10.1038/s41598-023-51017-z
20. Akbar N.S., Rafiq M., Muhammad T., et al. (2024). Biological structural study for the blood casson fluid flow in catheterized diverging tapered stenosed arteries with emerging shaped nanoparticles: application in drug delivery. *Microfluid. Nanofluid.* **28**:02735. DOI:10.1007/s10404-024-02735-x
21. Akbar N.S., Habib M.B., Rafiq M., et al. (2024). Biological structural study of emerging shaped nanoparticles for the blood flow in diverging tapered stenosed arteries to see their application in drug delivery. *Sci. Rep.* **14**:51848. DOI:10.1038/s41598-024-51848-4
22. Pattnaik P.K., Mishra S.R., Shamshuddin M., et al. (2024). Significant statistical model of heat transfer rate in radiative Carreau tri-hybrid nanofluid with entropy analysis using response surface methodology used in solar aircraft. *Renew. Energy* **237**:121521. DOI:10.1016/j.renene.2024.121521
23. Oreyeni T., Shamshuddin M.D., Obalalu A.M., et al. (2024). Exploring the impact of stratification fi cation on the dynamics of bioconvective thixotropic fluid conveying tiny particles and Cattaneo-Christov model: Thermal storage system application. *Propul. Power Res.* **13**:416–432. DOI:10.1016/j.jppr.2024.08.002
24. Sui Y., Lin H., Ding Z., et al. (2024). Compact, efficient, and affordable absorption Carnot battery for long-term renewable energy storage. *Appl. Energy* **357**:122504. DOI:10.1016/j.apenergy.2023.122504
25. Akbar N.S., Akram J., Hussain M.F., et al. (2024). Thermal storage study and enhancement of heat transfer through hybrid Jeffrey nanofluid flow in ducts under peristaltic motion with entropy generation. *Therm. Sci. Eng. Prog.* **49**:102463. DOI:10.1016/j.tsep.2024.102463
26. Dhange M., Devi C.U., Jamshed W., et al. (2024). Studying the effect of various types of chemical reactions on hydrodynamic properties of dispersion and peristaltic flow of couple-stress fluid: Comprehensive examination. *J. Mol. Liq.* **409**:125542. DOI:10.1016/j.molliq.2024.125542
27. Akbar N.S., Zamir T., Muhammad T. (2024). Levenberg-Marquardt technique analysis of thermal and concentration storage in cone-disk apparatus with neural network-enhancement. *Therm. Sci. Eng. Prog.* **50**:102529. DOI:10.1016/j.tsep.2024.102529
28. Akbar N.S., Zamir T., Akram J., et al. (2024). Simulation of hybrid boiling nano fluid flow with convective boundary conditions through a porous stretching sheet through Levenberg Marquardt artificial neural networks approach. *Int. J. Heat Mass Transf.* **228**:125615. DOI:10.1016/j.ijheatmasstransfer.2024.125615
29. Alghamdi M., Akbar N.S., Zamir T., et al. (2024). Double layered combined convective heated flow of Eyring-Powell fluid across an elevated stretched cylinder using intelligent computing approach. *Case Stud. Therm. Eng.* **54**:104009. DOI:10.1016/j.csite.2024.104009
30. Wang Y., Zhao J., Chen G., et al. (2018). A new understanding on thermal efficiency of organic Rankine cycle: Cycle separation based on working fluids properties. *Energy Conv. Manag.* **157**:169–175. DOI:10.1016/j.enconman.2017.11.079
31. Su W., Zhao L., Deng S., et al. (2018). A limiting efficiency of subcritical Organic Rankine cycle under the constraint of working fluids. *Energy* **143**:458–466. DOI:10.1016/j.energy.2017.11.003
32. Guo H., Xu Y., Li Y., et al. (2023). A symmetry analysis methodology for general energy conversion systems. *Commun. Eng.* **2**:49. DOI:10.1038/s44172-023-00096-x
33. Clapeyron É. (1834). Mémoire sur la puissance motrice de la chaleur. *J. École Polytech.* **23**:153–190.
34. Mollier R. (1923). Ein neues Diagramm fuer Dampf-luft-gemische. *Z. Ver. Dtsch. Ing.* **67**:869.
35. Gibbs J.W. (1928). The Collected Works of J. Willard Gibbs, Vol. 1:Thermodynamics (Yale University Press).
36. Nie X., Xue J., Zhao L., et al. (2024). New insight of thermodynamic cycle in thermoelectric power generation analyses: Literature review and perspectives. *Energy* **292**:130553. DOI:10.1016/j.energy.2024.130553
37. Chen R., Deng S., Xu W., et al. (2020). A graphic analysis method of electrochemical systems for low-grade heat harvesting from a perspective of thermodynamic cycles. *Energy* **191**:116547. DOI:10.1016/j.energy.2019.116547
38. Lu P., Luo X., Wang J., et al. (2022). Thermodynamic analysis and evaluation of a novel composition adjustable Carnot battery under variable operating scenarios. *Energy Conv. Manag.* **269**:116117. DOI:10.1016/j.enconman.2022.116117
39. Li J., Chen X., Shen J., et al. (2024). Optimal heat storage temperature and performance of ORC-based Carnot battery at various application scenarios. *Energy Conv. Manag.* **318**:118906. DOI:10.1016/j.enconman.2024.118906
40. Huang K., Chen R., Xu W., et al. (2024). Novel Graphical Expression Method of Thermodynamic Process Parameters: Methodology and Case Study. *Energy* **314**:134249. DOI:10.1016/j.energy.2024.134249
41. Bejan A. (2006). Advanced Engineering Thermodynamics, 3rd ed. (John Wiley & Sons).
42. Boltzmann L. (1877). Über die Natur der gasmoleküle. *Ann. Phys.* **236**:175–176. DOI:10.1002/andp.18772360120
43. Mayer J.R. (1842). Bemerkungen über die Kräfte der unbelebten Natur. *Liebigs Ann. Chem.* **236**:175–176. DOI:10.1002/andp.18772360120
44. Clausius R. (1850). Über die bewegende Kraft der Wärme und die Gesetze, welche sich daraus für die Wärmelehre selbst ableiten lassen. *Ann. Phys.* **155**:368–397. DOI:10.1002/andp.18501550306
45. Clausius R. (1865). The Mechanical Theory of Heat – with its Applications to the Steam Engine and to Physical Properties of Bodies (John van Voorst).
46. Ma Y. (2020). Effect of Finite-Size Heat Source's Heat Capacity on the Efficiency of Heat Engine. *Entropy* **22**:1002. DOI:10.3390/e22091002
47. Lu P., Luo X., Wang J., et al. (2022). Thermodynamic analysis and evaluation of a

novel composition adjustable Carnot battery under variable operating scenarios. *Energy Conv. Manag.* 269:116117. DOI:10.1016/j.enconman.2022.116117
48. Ishida M., Kawamura K. (1982). Energy and exergy analysis of a chemical process system with distributed parameters based on the enthalpy-direction factor diagram. *Ind. Eng. Chem. Process Des. Dev.* 21:690–695. DOI:10.1021/i200019a025
49. Zheng D., Wu Z., Huang W., et al. (2017). Energy quality factor of materials conversion and energy quality reference system. *Appl. Energy* 185:768–778. DOI:10.1016/j.apenergy.2016.10.103
50. Jiang X., Wang X., Feng L., et al. (2017). Adapted computational method of energy level and energy quality evolution for combined cooling, heating and power systems with energy storage units. *Energy* 120:209–216. DOI:10.1016/j.energy.2016.12.124
51. Wang Z., Han W., Zhang N., et al. (2018). Energy level difference graphic analysis method of combined cooling, heating and power systems. *Energy* 160:1069–1077. DOI:10.1016/j.energy.2018.07.026

FUNDING AND ACKNOWLEDGMENTS

This work is supported by the National Key R&D Program of China (No. SQ2024YFF0500207). The funders had no role in study design, data collection and analysis, decision to publish, or preparation of the manuscript.

AUTHOR CONTRIBUTIONS

Kunteng Huang: Software, Data curation, Writing-original draft. **Zhixin Huang:** Methodology, Writing-review & editing; **Ruihua Chen:** Methodology, Visualization. **Ruizhao Gao:** Methodology, review & editing; **Hao Wang:** Visualization; **Weicong Xu:** Formal analysis; **Shuai Deng:** Visualization; **Li Zhao:** Conceptualization, Investigation; All authors contributed to the manuscript and approved the final version.

DECLARATION OF INTERESTS

The authors declare no competing interests.

DATA AND CODE AVAILABILITY

Data are available from the corresponding author upon reasonable request.

SUPPLEMENTAL INFORMATION

It can be found online at https://doi.org/10.59717/j.xinn-energy.2025.100084